

# Investigating the Semantic Robustness of CLIP-based Zero-Shot Anomaly Segmentation

Kevin Stangl\*  
TTIC, USA

kevin@ttic.edu

Marius Arvinte Weilin Xu Cory Cornelius  
Intel Labs, USA

firstname.lastname@intel.com

## Abstract

Zero-shot anomaly segmentation using pre-trained foundation models is a promising approach that enables effective algorithms without expensive, domain-specific training or fine-tuning. Ensuring that these methods work across various environmental conditions and are robust to distribution shifts is an open problem. We investigate the performance of WinCLIP [14] zero-shot anomaly segmentation algorithm by perturbing test data using three semantic transformations: bounded angular rotations, bounded saturation shifts, and hue shifts. We empirically measure a lower performance bound by aggregating across per-sample worst-case perturbations and find that average performance drops by up to 20% in area under the ROC curve and 40% in area under the per-region overlap curve. We find that performance is consistently lowered on three CLIP backbones, regardless of model architecture or learning objective, demonstrating a need for careful performance evaluation.

## 1. Introduction

Visual anomaly segmentation is a challenging and important task, especially in manufacturing line applications, where objects have to be inspected in a fast, automated way, that is robust under a varied number of environmental conditions [3, 32]. Anomalies manifest as fabrication defects (scratches, chips) and localizing them using fine-grained segmentation allows for interpretability of different types of defects [3]. Given the variety of items that are inspected, collecting large, annotated training sets for each object is prohibitive. Even if data would be available, training and deploying separate models for each object is costly.

\*Work done while at Intel Labs, USA.

This publication includes work that was funded by the Government under the Defense Advanced Research Projects Agency (DARPA) Guaranteeing AI Robustness against Deception (GARD) Program, Agreement #HR00112030001.

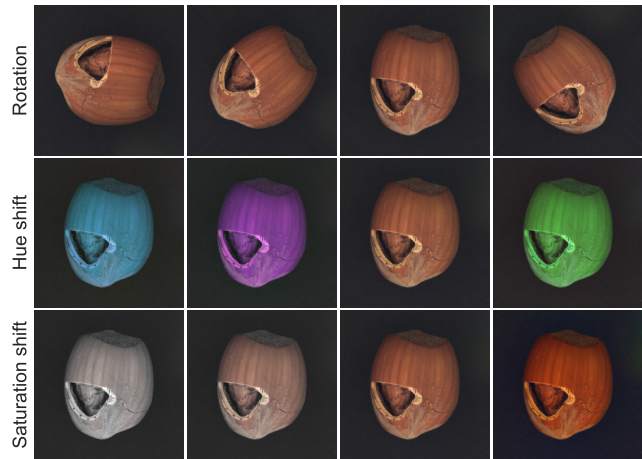


Figure 1. Effects of the three augmentations applied to the same anomalous (a large crack in the shell of a hazelnut) MVTec sample. The third column represents the original sample.

Recent work [14, 31] leverages the zero-shot generalization ability of foundation models [21] to address anomaly segmentation across a varied number of objects and environments. A modern line of work in computer vision deals with test-time robustness of discriminative models against natural distribution shifts [7, 10], where it is found that, generally, even large-scale models are fragile to well-chosen, per-sample perturbations. This has been recently demonstrated for CLIP-based models both for the case of noise-like perturbations [23] and for natural perturbations (such as camera pose changes) [26].

In this work, we investigate the robustness of downstream anomaly segmentation using CLIP when faced with three perturbations (rotations, hue shift, saturation shift) that simulate naturally occurring distribution shifts. Importantly, we bound these shifts in a controlled way such that anomalies remain clearly present when inspected by humans – the question we investigate is *if CLIP-based anomaly segmentation is invariant to these shifts?*

Our results demonstrate that average segmentation per-

formance is reduced across most objects across CLIP backbones, with drops of up to 40% in the per-sample worst-case setting. This performance drop points to the need of conducting lower bound performance evaluations of foundation models used in zero-shot anomaly segmentation, and is in line with a recent line of work that investigates the resilience of foundation models to natural distribution shifts and adversarial examples [15, 24].

### 1.1. Related Work

A large number of recent works have introduced zero-shot anomaly classification and segmentation algorithms that use foundation models [5, 6, 9, 12, 30]. Among these, we focus on WinCLIP [14] because of its good performance, fast inference speed, and open-source implementation in the `anomalib` library [1]. WinCLIP for anomaly segmentation has two components: a template-based prompting strategy, and a multi-scale pooling strategy to aggregate information across multiple spatial scales. Other recent methods have used the properties of diffusion processes for anomaly detection [19], pre-trained diffusion models [30], and vision-language models [9].

Recent work [24, 27] investigates the robustness of CLIP and how previously reported results likely over-state the observed effective robustness due to evaluating on a static test set from one distribution. The work in Idrissi et al. [13] characterizes subsets of the ImageNet dataset and identifies color shifts as a common subset and potential augmentation.

Our proposed work is similar in spirit to both previous idea, given that we propose to evaluate anomaly segmentation on worst-case augmented samples from the original test set, and our augmentations include color shifts [4, 11]. Another line of work [17, 26, 28] questions whether CLIP suffers from inaccurate physical grounding, showing that semantic properties of images are not understood by vision-language models such as LLaVA [18] or GPT-4V [20].

## 2. Methods

To investigate the performance of anomaly segmentation under worst-case distribution shifts, we use three semantic preserving augmentations: rotation, hue shift, and saturation shift. Their effects on the same sample are shown in Figure 1, where it can be seen that the anomaly remains detectable across the entire augmentation range.

The query sample  $x$  is clockwise rotated using an angle  $\theta$ , followed by an RGB to HSV conversion. Additive shifts  $\delta_h$  and  $\delta_s$  are independently applied to the hue and saturation channels [11], respectively, after which the sample is converted back to its RGB representation, yielding the augmented sample  $x_{\text{aug}}$ . The pre-processing is summarized as:

$$x_{\text{aug}} = f(x; \theta, \delta_h, \delta_s). \quad (1)$$

The modified sample  $x_{\text{aug}}$  is input to zero-shot anomaly detection using WinCLIP [14], yielding the estimated soft (continuous) anomaly maps  $\tilde{y}_{\text{aug}}$  as:

$$\tilde{y}_{\text{aug}} = w(x_{\text{aug}}). \quad (2)$$

Finally, the output sensitivity maps are additionally rotated counter-clockwise using the angle  $\theta$  (hue and saturation shifts do not spatially change the sample) to yield:

$$\tilde{y} = f(\tilde{y}_{\text{aug}}; -\theta, 0, 0), \quad (3)$$

where the choice of  $\delta_h = \delta_s = 0$  implies there is no HSV space conversion performed. This allows for fair end-to-end comparison between  $\tilde{y}$  and the ground-truth segmentation maps  $y$ , without requiring any intervention on  $y$ .

The entire pre-processing pipeline is differentiable, thus the parameters  $\theta, \delta_h, \delta_s$  can be optimized using gradient-based methods. However, doing so on a per-sample basis requires defining a differentiable loss function that measures anomaly segmentation loss. We introduce the following simplified version of the Dice loss [25] (using the  $\ell_1$ -norm) from medical image segmentation:

$$l(\tilde{y}, y) = \frac{\sum_i \tilde{y}_i(1 - y_i)}{\sum_i (1 - y_i) + \epsilon} - \frac{\sum_i \tilde{y}_i y_i}{\sum_i y_i + \epsilon}, \quad (4)$$

where  $\epsilon = 1e-8$  is a small constant added for numerical stability.

Note that this is a valid segmentation loss: the first term encourages low values for  $\tilde{y}_i$ , where  $i$  satisfies  $y_i = 0$  (i.e., true negative pixels). Similarly, the second term encourages higher values of  $\tilde{y}_i$  for the true positive pixels. Unlike the Dice loss, our proposed loss does not contain the estimated output  $\tilde{y}$  in the denominator, which improves numerical stability when back-propagating gradients to the inputs.

Unlike supervised learning (where the goal is loss minimization), the goal of our work is to *maximize* this loss by optimizing the three parameters  $\theta, \delta_h, \delta_s$  as:

$$\begin{aligned} \theta^*, \delta_h^*, \delta_s^* &= \operatorname{argmax}_{\theta, \delta_h, \delta_s} l(\tilde{y}(\theta, \delta_h, \delta_s), y), \\ \text{s.t. } \theta &\in [-90^\circ, 90^\circ], \delta_s \in [-0.5, 0.5]. \end{aligned} \quad (5)$$

To obtain the tightest lower performance bounds, this optimization is done separately for each sample in the test set. We used the Adam optimizer [16] with at most 200 optimization steps per sample to approximate the solution to (5). Details are provided in the supplementary material.

The above is an approximation of the worst-case setting encountered in practice across an extended period of time: every individual test sample is manipulated in its own worst way (by accident or ill-intended) with respect to the downstream task, while still ensuring that the manipulation is realistic and preserves the semantic information of the sample

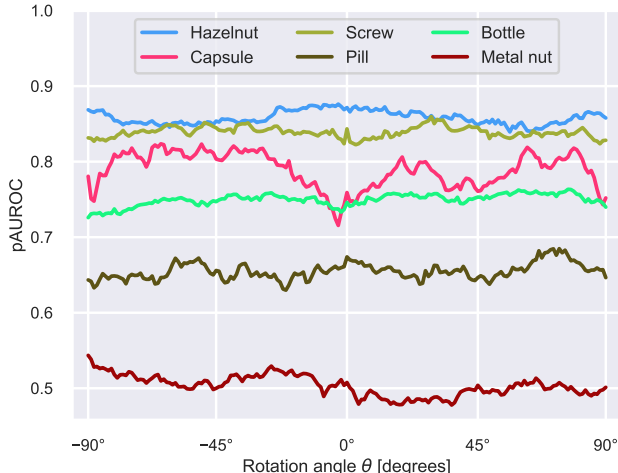


Figure 2. Zero-shot anomaly segmentation performance when the same rotation angle  $\theta$  is applied to the MVTec test set for rotation-invariant objects.

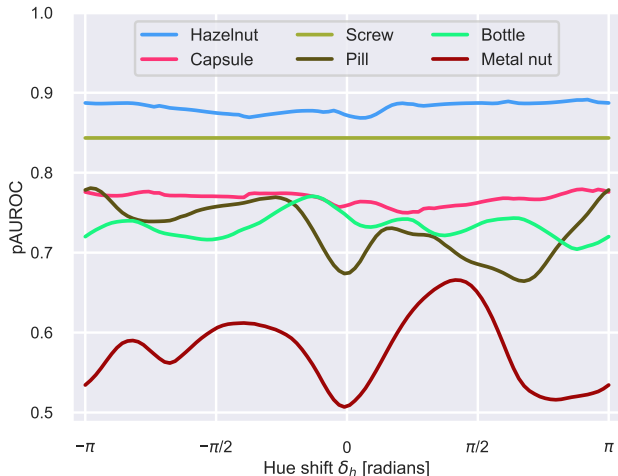


Figure 3. Zero-shot anomaly segmentation performance when the same additive (modulo  $2\pi$ ) hue shift  $\delta_h$  is applied to the MVTec test set for rotation-invariant objects.

(e.g., using a bounded saturation shift). Samples are aggregated and final performance is measured using three metrics, following the protocol described in Jeong et al. [14]: pixel-level area under the ROC curve (pAUROC), area under the per-region overlap curve (AUPRO), and the  $F_1$ -max score.

### 3. Experimental Results and Discussion

#### 3.1. Uniform lower performance bounds

We first evaluate the performance of zero-shot anomaly segmentation when only one of the three augmentations is applied *using the same value* to the entire test set. This is a

loose lower bound, but we find that even in this case, conclusions are non-trivial.

Figure 2 shows zero-shot segmentation pAUROC for six objects in the MVTec dataset when the same rotation angle  $\theta$  is applied to all test samples using the protocol in Section 2. Only objects that are placed on matte backgrounds were chosen for evaluation, to ensure that rotation does not produce artificial anomalies in the corners of  $x_{\text{aug}}$ . Figure 2 reveals that rotating samples has a non-trivial and non-smooth effect on downstream task performance: small rotations at arbitrary angles can cause a performance difference of up to 3% in pAUROC to appear in most objects. Performance can vary by up to 10% between the lower and upper bounds of a certain object (e.g., for capsule). Similar results for the VisA dataset are in the supplementary material.

Figure 3 shows zero-shot segmentation pAUROC the same six objects in Figure 2 when the same hue shift  $\delta_h$  is applied to the test samples. In this case, variations are smoother, but effects are still non-trivial: certain objects are less sensitive (e.g., all screw images are gray-scale, and completely unaffected by hue), while others show a significant performance variation (e.g., pill and metal nut) of up to 15%. Given that hue shifts should not affect physical defects in objects, this indicates that the backbone used here (ViT-B/16+) is not sufficiently robust to these shifts, even when the shifts are not sample-specific.

#### 3.2. Per-sample lower performance bounds

We report per-sample lower performance bounds where the worst-case transformation is independently obtained for each test sample, followed by aggregating all augmented samples and reporting performance.

As expected from Figure 2, the distribution of worst-case angles across individual samples is approximately uniform: given that only rotation-invariant objects were evaluated, there is no reason for specific angles to be systematically worst-case for all samples. The distribution is shown in the supplementary material.

Figure 4 shows the distribution of performance drops across objects for three CLIP backbones tested on both the augmented MVTec and VisA datasets. Four per-sample worst-case augmentations were used: three one-dimensional ones – in angle  $\theta$ , hue shift  $\delta_h$ , saturation shift  $\delta_s$  – and the worst-case lower performance bound obtained by jointly optimizing all three variables for each sample and aggregating results. In general, we notice that the lower bound is looser (performance suffers a larger drop) for the VisA dataset compared to MVTec in the case of non-adversarially fine-tuned backbones. When considering that VisA is a more difficult test set than MVTec (based on the lower original performance in Table 1), the even higher worst-case performance drop indicates that a significant robustness gap exists in harder segmentation problems.

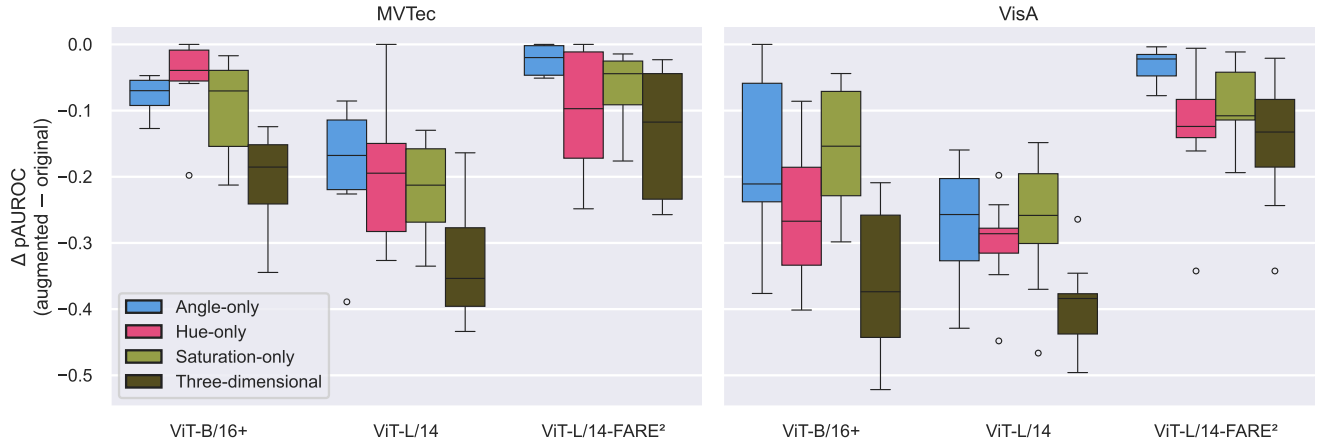


Figure 4. Zero-shot anomaly segmentation performance for two datasets (MVTec and VisA, left and right, respectively) using three CLIP backbones (ViT-B/16+, ViT-L/14, and adversarially fine-tuned ViT-L/14-FARE<sup>2</sup> for WinCLIP. The three test-time, worst-case semantic perturbations (angle, saturation, hue) are considered either separately, or simultaneously (3D). The bars show the difference between the original test sets and the considered lower bounds.

Anomaly Segmentation		MVTec-AD				VisA			
Eval. data	Backbone	pAUROC	AUPRO	$F_1$ -max	Loss	pAUROC	AUPRO	$F_1$ -max	Loss
Original	ViT-B/16+	80.1	64.2	24.1	0.075	76.4	55.4	10.9	0.165
	ViT-L/14	59.1	21.9	9.9	0.108	59.3	26.3	2.89	0.199
	ViT-L/14-FARE <sup>2</sup>	37.7	10.6	8.3	0.108	30.6	4.81	2.10	0.203
Per-sample	ViT-B/16+	59.8	23.6	12.8	0.085	40.3	16.0	2.28	0.180
3D lower	ViT-L/14	26.4	4.25	7.68	0.115	19.9	3.59	1.37	0.210
bound	ViT-L/14-FARE <sup>2</sup>	24.2	3.54	7.80	0.111	16.5	2.12	1.37	0.208

Table 1. Anomaly segmentation performance under the original test data and the per-sample worst-case lower bound.

In terms of specific one-dimensional perturbations, hue shifts affect VisA the most on average (across all backbones), while the results for MVTec are less conclusive, and more backbone-dependent. The adversarially fine-tuned FARE<sup>2</sup> backbone [23] consistently shows lower performance drops, but the nominal performance also suffers a significant drop, indicating a sharp trade-off between robustness to distribution shifts and absolute performance.

Table 1 shows results for anomaly segmentation metrics, evaluated on both datasets, using three models. We compare the original (un-augmented) test set performance with that of the worst-case per-sample lower bound. Given the imbalanced nature of anomaly segmentation (fewer positive pixels than negatives), the AUPRO scores suffers a performance of up to 40% using the ViT-B/16+ architecture. Similarly, we reproduce the already-low  $F_1$ -max score on the original test sets, and this value drop to as low as 2% for the VisA dataset using the ViT-B/16+ architecture. Table 1 shows the numerical values of the optimization objective defined in (4) used to find worst-case augmentations: it can

be seen that the values are inversely correlated with the performance metrics, and that (4) is a valid segmentation loss.

## 4. Conclusion

Our work demonstrates the generalization challenges of zero-shot anomaly segmentation algorithms when faced with relatively simple test-time augmentations (rotation, hue, saturation). By formulating an optimization problem that determines the per-sample worst-case augmentations, we show performance drops for CLIP-based anomaly segmentation of up to 40% in pAUROC compared to the original test set.

Standard practice for CLIP pre-trained models is to not use heavy augmentation pipelines [21] – some samples have text label information about their color, which would make naive color augmentations not compatible with the learning objective. Future research could consider how to generalize semantic augmentations to multi-modal data and include this in the training of foundation models. Finally, all our work targeted zero-shot anomaly segmentation. Few-shot



anomaly segmentation is common in practice and significant improvements could be achieved if test-time augmentations were optimized to *maximize* performance for each object type instead of minimizing it, as we did in this work.

## References

- [1] Samet Akcay, Dick Ameln, Ashwin Vaidya, Barath Lakshmanan, Nilesh Ahuja, and Utku Genc. Anomalib: A deep learning library for anomaly detection. In *2022 IEEE International Conference on Image Processing (ICIP)*, pages 1706–1710. IEEE, 2022. 2
- [2] Yoshua Bengio, Nicholas Léonard, and Aaron Courville. Estimating or propagating gradients through stochastic neurons for conditional computation. *arXiv preprint arXiv:1308.3432*, 2013. 1
- [3] Paul Bergmann, Michael Fauser, David Sattlegger, and Carsten Steger. Mvtec ad—a comprehensive real-world dataset for unsupervised anomaly detection. In *Proceedings of the IEEE/CVF conference on computer vision and pattern recognition*, pages 9592–9600, 2019. 1
- [4] Anand Bhattad, Min Jin Chong, Kaizhao Liang, Bo Li, and D. A. Forsyth. Unrestricted adversarial examples via semantic manipulation, 2020. 2
- [5] Yunkang Cao, Xiaohao Xu, Chen Sun, Yuqi Cheng, Zongwei Du, Liang Gao, and Weiming Shen. Segment any anomaly without training via hybrid prompt regularization. *arXiv preprint arXiv:2305.10724*, 2023. 2
- [6] Yunkang Cao, Xiaohao Xu, Chen Sun, Xiaonan Huang, and Weiming Shen. Towards generic anomaly detection and understanding: Large-scale visual-linguistic model (gpt-4v) takes the lead. *arXiv preprint arXiv:2311.02782*, 2023. 2
- [7] Xinquan Chen, Xitong Gao, Juanjuan Zhao, Kejiang Ye, and Cheng-Zhong Xu. Advdiffuser: Natural adversarial example synthesis with diffusion models. In *Proceedings of the IEEE/CVF International Conference on Computer Vision*, pages 4562–4572, 2023. 1
- [8] Thomas Eboli. High-quality pytorch image and volume rotation. Accessed on April 24, 2024. 1
- [9] Zhaopeng Gu, Bingke Zhu, Guibo Zhu, Yingying Chen, Ming Tang, and Jinqiao Wang. Anomalygpt: Detecting industrial anomalies using large vision-language models. In *Proceedings of the AAAI Conference on Artificial Intelligence*, pages 1932–1940, 2024. 2
- [10] Dan Hendrycks, Kevin Zhao, Steven Basart, Jacob Steinhardt, and Dawn Song. Natural adversarial examples. In *Proceedings of the IEEE/CVF conference on computer vision and pattern recognition*, pages 15262–15271, 2021. 1
- [11] Hossein Hosseini and Radha Poovendran. Semantic adversarial examples. In *Proceedings of the IEEE Conference on Computer Vision and Pattern Recognition Workshops*, pages 1614–1619, 2018. 2
- [12] Chaoqin Huang, Haoyan Guan, Aofan Jiang, Ya Zhang, Michael Spratling, and Yan-Feng Wang. Registration based few-shot anomaly detection, 2022. 2
- [13] Badr Youbi Idrissi, Diane Bouchacourt, Randall Balestriero, Ivan Evtimov, Caner Hazirbas, Nicolas Ballas, Pascal Vincent, Michal Drozdal, David Lopez-Paz, and Mark Ibrahim. Imagenet-x: Understanding model mistakes with factor of variation annotations. *arXiv preprint arXiv:2211.01866*, 2022. 2
- [14] Jongheon Jeong, Yang Zou, Taewan Kim, Dongqing Zhang, Avinash Ravichandran, and Onkar Dabeer. Winclip: Zero-/few-shot anomaly classification and segmentation, 2023. 1, 2, 3
- [15] Nikhil Kandpal, Matthew Jagielski, Florian Tramèr, and Nicholas Carlini. Backdoor attacks for in-context learning with language models, 2023. 2
- [16] Diederik P Kingma and Jimmy Ba. Adam: A method for stochastic optimization. *arXiv preprint arXiv:1412.6980*, 2014. 2, 1
- [17] Martha Lewis, Nihal V. Nayak, Peilin Yu, Qinan Yu, Jack Merullo, Stephen H. Bach, and Ellie Pavlick. Does clip bind concepts? probing compositionality in large image models, 2023. 2
- [18] Haotian Liu, Chunyuan Li, Qingyang Wu, and Yong Jae Lee. Visual instruction tuning. In *Thirty-seventh Conference on Neural Information Processing Systems*, 2023. 2
- [19] Victor Liversoche, Vineet Jain, Yashar Hezaveh, and Siamak Ravanbakhsh. On diffusion modeling for anomaly detection. *arXiv preprint arXiv:2305.18593*, 2023. 2
- [20] OpenAI. Gpt-4 technical report, 2024. 2
- [21] Alec Radford, Jong Wook Kim, Chris Hallacy, Aditya Ramesh, Gabriel Goh, Sandhini Agarwal, Girish Sastry, Amanda Askell, Pamela Mishkin, Jack Clark, Gretchen Krueger, and Ilya Sutskever. Learning transferable visual models from natural language supervision, 2021. 1, 4
- [22] E. Riba, D. Mishkin, D. Ponsa, E. Rublee, and G. Bradski. Kornia: an open source differentiable computer vision library for pytorch. In *Winter Conference on Applications of Computer Vision*, 2020. 1
- [23] Christian Schlarmann, Naman Deep Singh, Francesco Croce, and Matthias Hein. Robust clip: Unsupervised adversarial fine-tuning of vision embeddings for robust large vision-language models, 2024. 1, 4
- [24] Zhouxing Shi, Nicholas Carlini, Ananth Balashankar, Ludwig Schmidt, Cho-Jui Hsieh, Alex Beutel, and Yao Qin. Effective robustness against natural distribution shifts for models with different training data. *arXiv preprint arXiv:2302.01381*, 2023. 2
- [25] Carole H. Sudre, Wenqi Li, Tom Vercauteren, Sebastien Ourselin, and M. Jorge Cardoso. *Generalised Dice Overlap as a Deep Learning Loss Function for Highly Unbalanced Segmentations*, page 240–248. Springer International Publishing, 2017. 2
- [26] Shengbang Tong, Zhuang Liu, Yuexiang Zhai, Yi Ma, Yann LeCun, and Saining Xie. Eyes wide shut? exploring the visual shortcomings of multimodal llms. *arXiv preprint arXiv:2401.06209*, 2024. 1, 2
- [27] Weijie Tu, Weijian Deng, and Tom Gedeon. A closer look at the robustness of contrastive language-image pre-training (clip). *Advances in Neural Information Processing Systems*, 36, 2024. 2
- [28] Vishaal Udandarao, Max F. Burg, Samuel Albanie, and Matthias Bethge. Visual data-type understanding does not emerge from scaling vision-language models, 2023. 2

- [29] Michael Unser, Philippe Thevenaz, and Leonid Yaroslavsky. Convolution-based interpolation for fast, high-quality rotation of images. *IEEE Transactions on image processing*, 4(10):1371–1381, 1995. [1](#)
- [30] Julian Wyatt, Adam Leach, Sebastian M Schmon, and Chris G Willcocks. Anoddpm: Anomaly detection with denoising diffusion probabilistic models using simplex noise. In *Proceedings of the IEEE/CVF Conference on Computer Vision and Pattern Recognition*, pages 650–656, 2022. [2](#)
- [31] Qihang Zhou, Guansong Pang, Yu Tian, Shibo He, and Jiming Chen. Anomalyclip: Object-agnostic prompt learning for zero-shot anomaly detection. *arXiv preprint arXiv:2310.18961*, 2023. [1](#)
- [32] Yang Zou, Jongheon Jeong, Latha Pemula, Dongqing Zhang, and Onkar Dabeer. Spot-the-difference self-supervised pre-training for anomaly detection and segmentation, 2022. [1](#)

# Investigating the Semantic Robustness of CLIP-based Zero-Shot Anomaly Segmentation

## Supplementary Material

### A. Implementation Details

#### A.1. Augmentations

To implement the rotation augmentation, we used the three-pass convolutional approach from Unser et al. [29]. Compared to bilinear interpolation, this method preserves the high-frequency content of the samples and ensures that minimal distortions (at least when evaluated by humans) are introduced via the rotation. To extrapolate pixels in the corners of the rotated sample, we used the `replicate` padding mode: for each extrapolated pixel, the value of the nearest pixel from the rotated sample itself is copied. We used the `torch-rotation` library [8] to implement the differentiable three-pass rotation.

Hue and saturation shifts were implemented using the RGB-to-HSV conversion function from the `kornia` library [22], with the shifts themselves being otherwise straightforward to implement.

Given that saturation is clipped to  $[0, 1]$  after the shift is applied, we used a straight-through estimator (STE) [2] to back-propagate through this operation even outside its valid range. Similarly, we used the STE estimator to clip and back-propagate the values of the rotation angle  $\theta$  and saturation shift  $\delta_s$  whenever they exceed their permitted ranges.

#### A.2. Solving the optimization problem

We used the Adam optimizer [16] with learning rates of 5 for  $\theta$  and 0.1 for  $\delta_h$  and  $\delta_s$ , respectively. The learning rates were chosen based on the  $\ell_\infty$ -norm of the gradient with respect to each variable at initialization, and were not extensively fine-tuned or searched for.

We found that using random restarts and for the optimization problem is crucial for successfully decreasing the per-sample lower performance bound. In particular, the loss surface is highly non-convex for the angle  $\theta$ , and optimization often gets trapped in local minima. Given the relatively low budget of 200 steps, we used 5 restarts: the first optimization run starts with the default values  $\theta = \delta_h = \delta_s = 0$ , while the subsequent four runs restart these values using uniform sampling from the valid interval of each variable.

Additionally, we also monitor the per-sample segmentation pAUROC for samples that have at least one anomalous labeled pixel in  $y$  and select the specific perturbations  $(\theta^*, \delta_h^*, \delta_s^*)$  that minimize this value. Note that this is still sub-optimal when it comes to minimizing the pAUROC on pixels from all samples of a specific object, which is generally intractable. Finally, for samples that have  $y_i = 0$  for

all  $i$  (no anomalous pixels), we monitor the loss function  $L$  in (4) and select the specific perturbations  $(\theta^*, \delta_h^*, \delta_s^*)$  that maximize this value.

#### A.3. Selecting rotation-invariant objects

To select rotation-invariant objects, we used the per-pixel average mean squared error between the extrapolated corner pixels using our rotation method and the original corner pixels as:

$$e(x) = \frac{\sum_i m_i \cdot (x_i - f(x_i; \theta = 45^\circ))^2}{\sum_i m_i}, \quad (6)$$

where  $m_i$  is a binary mask that indicates whether a specific pixel was extrapolated or not and is obtained by rotating a monochrome image with maximum pixel intensity. We evaluate this error using the specific angle  $\theta = 45^\circ$ , with the reasoning that it is where the most extrapolation occurs, and rotation-invariant objects should not be cut-off by this rotation. If a cut-off would occur, the object texture would be reflected in the extrapolated corner, thus producing a high error compared to the original corner region.

The above is followed by a manual thresholding of the error, as well as final careful visual inspection of the down-selected classes. Tables 2 and 3 show the selection results for objects in the MVTEC and VisA datasets, respectively.

#### A.4. Optimization outcomes

Figure 5 shows the histogram of per-sample worst-case rotation angles  $\theta^*$  when optimizing only for rotation. The higher mode around the origin is due to the intentional artifacts introduced when de-rotating the estimated anomaly map  $\tilde{y}_{\text{aug}}$ : for difficult samples, this may cause a slight performance boost at any rotation angle. This causes the optimization in (5) to return a near-zero angle as the worst-case one.

### B. Additional uniform lower bound results

Figure 6 shows the results for applying the same saturation shift  $\delta_s$  to all samples in the MVTEC test set. Similar to the result for the hue shift  $\delta_h$  in Figure 3, there are significant performance variations for most objects except metal nut, which already contains gray-scale samples that are less sensitive to color shifts.

Figures 7, 8, and 9 show the uniform lower bounds obtained from applying the same rotation, hue shift, or saturation shift to all test samples in the VisA dataset, respectively.

Object name	Corner MSE	Used
Metal nut	0.000255	True
Pill	0.000304	True
Hazelnut	0.000391	True
Bottle	0.002179	True
Screw	0.005964	True
Leather	0.013949	False
Wood	0.021015	False
Capsule	0.02621	True
Cable	0.027923	False
Transistor	0.077574	False
Tile	0.09312	False
Carpet	0.104486	False
Grid	0.126188	False
Toothbrush	0.17937	False
Zipper	0.92926	False

Table 2. Average corner extrapolation MSE for objects in the MVTec dataset. *Leather* and *wood* were excluded from evaluation after manual inspection, given that the textures span the entire sample and simple extrapolation would lead to qualitative artifacts in the samples that could be mistaken for anomalies.

Object name	Corner MSE	Used
Pipe fryum	0.000668	True
Pcb3	0.001449	True
Macaroni1	0.004837	True
Pcb4	0.005264	True
Fryum	0.00995	True
Pcb2	0.010521	True
Pcb1	0.013953	True
Chewing gum	0.024117	True
Macaroni2	0.035739	True
Cashew	0.049281	True
Candle	0.051116	False
Capsules	0.082838	False

Table 3. Average corner extrapolation MSE for objects in the VisA dataset.

While the same conclusions related to how smooth performance varies with each augmentation type (noisy for rotations, smooth for color shifts), the dynamic ranges of the per-object performance are much larger for VisA, which is generally a more difficult dataset. For certain objects, such as *Pcb1* or *Macaroni1*, performance can vary by up to 0.4 points in pAUROC when rotations or hue shifts are applied, respectively.

### C. Additional worst-case lower bound results

Figure 10 shows the results for worst-case lower bounds obtained by jointly optimizing any combination of considered augmentations. In general, we note that augmentations that



Figure 5. Empirical distribution of per-sample worst-case rotation angles for all rotationally invariant objects in MVTec. The slight peak around the origin is caused by the optimization being sub-optimal due to the de-rotation of  $\tilde{y}_{aug}$  using zero value extrapolation in the corners.

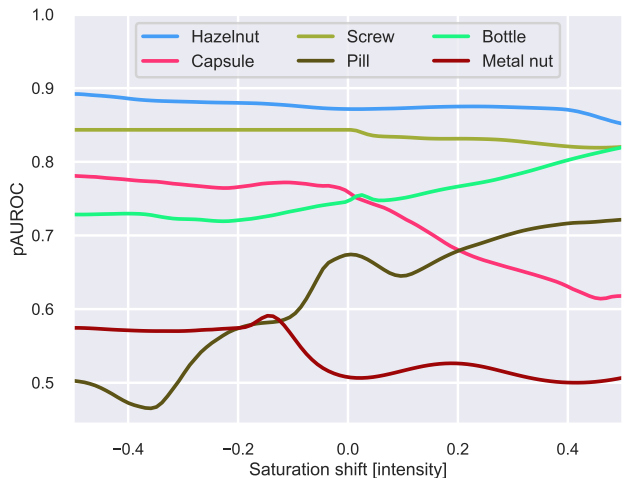


Figure 6. Zero-shot anomaly segmentation performance when the same saturation shift  $\delta_s$  is applied to the MVTec test set for rotation-invariant objects.

only involve colours (hue and saturation) are more effective (leads to a higher performance drop) than the ones involving the rotation augmentation. We attribute this to the non-smooth optimization surface for the rotation angle  $\theta$ , which holds even under our considered segmentation loss.



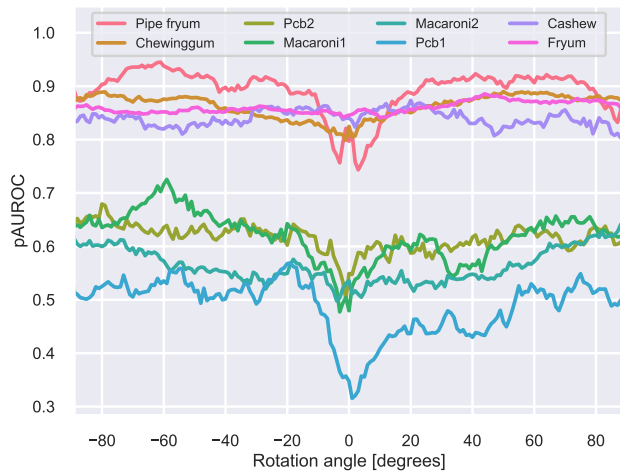


Figure 7. Zero-shot anomaly segmentation performance when the same rotation angle  $\theta$  is applied to the VisA test set for rotation-invariant objects.

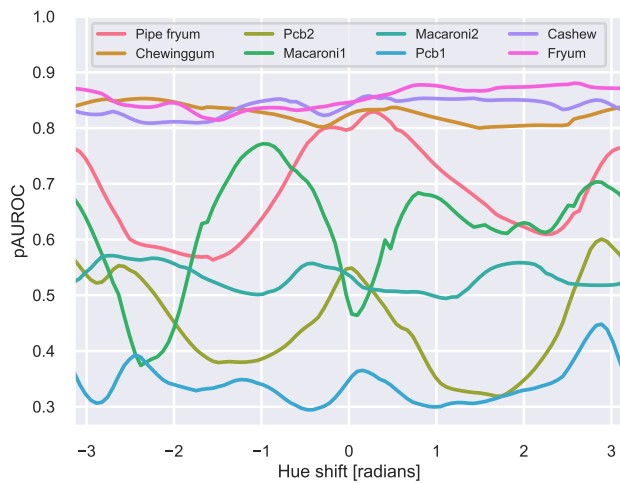


Figure 8. Zero-shot anomaly segmentation performance when the same hue shift  $\delta_h$  is applied to the VisA test set for rotation-invariant objects.

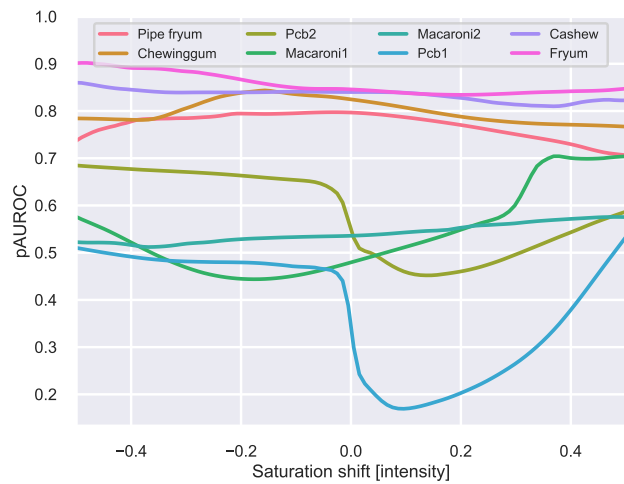


Figure 9. Zero-shot anomaly segmentation performance when the same saturation shift  $\delta_s$  is applied to the VisA test set for rotation-invariant objects.

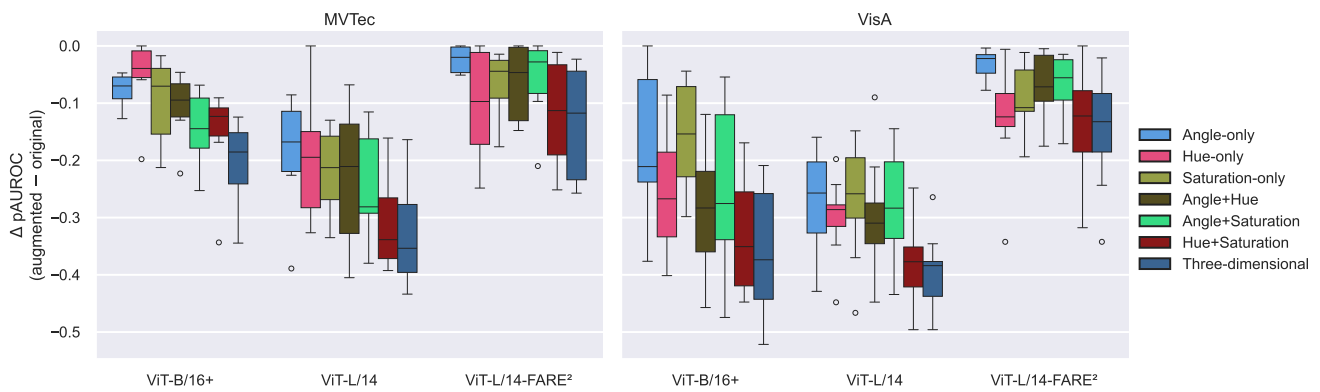


Figure 10. Zero-shot anomaly segmentation performance for two datasets (MVTEC and VisA, left and right, respectively) using three CLIP backbones (ViT-B/16+, ViT-L/14, and adversarially fine-tuned ViT-L/14-FARE<sup>2</sup> for WinCLIP). Each possible combination of the three test-time, worst-case semantic perturbations (angle, saturation, hue) is considered, to yield a set of eight total test-time augmentation strategies. The bars show the difference between the original test sets and the considered lower bounds. This figure complements Figure 4 in the main body.